Efficient modeling of masonry failure using a multiscale domain activation approach

Efficient Modeling of Masonry Failure using a Multiscale Domain Activation Approach

Cedric Driesen[1,*], Hervé Degée[1], Bram Vandoren[1,1]

Construction Engineering Research Group, Hasselt University, 3500 Hasselt, Belgium

Abstract

A finite element based framework that formulates an adaptive multiresolution multiscale technique is presented, with the goal of both accurately and efficiently simulating large masonry structures. In order to find a compromise between accuracy and computational efficiency a scale embedding multiscale model where both macro- and microscale elements come into play is proposed, combining the advantages both have to offer. This theory is tested and compared with an equivalent microscale model to demonstrate that its accuracy rivals a microscale approach, while at the same time having a higher computational efficiency. The developed multiscale model is compared to its underlying microscale model in a couple of selected example structures, ranging from small to large scale unreinforced masonry walls with openings. An application in the form of soil subsidence is explored, showing a potential for extended applications of this type of modeling.

Keywords: Masonry, Finite Element, Multiscale

[*]Corresponding author: cedric.driesen@uhasselt.be

[1]bram.vandoren@uhasselt.be

1. Introduction

The complexity of masonry lies in its constituents: brick units and mortar joints, which are organized on a relatively small scale. These materials form a complex arrangement which proves itself difficult to model due to the large amount of units that make up even a small scale construction. The second major difficulty with masonry, which is actually quasi-brittle, is the complex global structural response due to its arrangement. Both these issues can cause significant computational problems. So, the existence of many different units and joints means that to accurately model even a medium scale structure will take up a considerable amount of runtime.

The basic main modeling techniques used in masonry [1, 2, 3, 4] are the detailed microscale method, the simplified microscale method, and the macroscale method, all often implemented using a variation of the Finite Element Method (FEM). These three methods are shown in Figure 2 for a simple 2D masonry system. In many comparisons these modeling methods are successfully applied with good comparison to experimental results [5].

In the detailed microscale approach it is possible to take into account the Poisson's ratio and Young modulus of the mortar joint, which cannot be done explicitly in the simplified microscale method. The properties of the brick units are, however, taken into account in both methods. The interface separating brick and mortar in the detailed microscale or expanded brick elements in the simplified microscale approach represent a plane which can undergo damage, leading to cracking and failure. It is the combination of these simpler linear elastic elements and the non-linear interfaces which leads to a potentially accurate computational representation of masonry. On the other hand there is the macroscale model. In this approach one models the entire masonry material into one element type, chosen to be either linear or non-linear depending on the application. Capturing the behavior of the detailed masonry geometry into these larger elements is called homogenization. There has been a lot of research into the analytical or computational homogenization of masonry [6, 7, 8], especially for masonry with a periodic geometry [9, 10, 11]. In a periodic construction one can choose the Representative Volume Element (RVE), which is the detailed geometry captured in the macroscale element, in such a way that the RVE for each macroscale element is the same, simplifying the homogenization process. Analytical or semi-analytical methods were developed for in-plane and out-of-plane loading, and these methods have been successfully applied in finding the elastic

response of masonry structures with periodic geometries [12]. On the other hand, computational models determining the elastic behavior have also been developed [13]. For non-elastic responses, one must implement the non-linear effects of damage into the macroscale constitutive laws, which can be done in many ways, using damage or plasticity relations [14, 15, 16].

In most use cases, assuming choosing regular brick and mortar types, nonlinear effects (in this case damage propagation) is more likely to occur in the mortar joints than in the brick itself [1]. Even when damage occurs in the brick it is mainly localized between two vertical mortar joints. The most likely locations where damage would occur can be seen in Figure 1. The damage localization led to the development of the simplified microscale methods, which sometimes include other less likely cracking paths.

The simplest way to homogenize the microscopic behavior is to neglect any non-linear effects and assume a perfectly elastic response [13]. Because this work assumes that all the non-linear behavior will be captured in the microscale model, the focus is on these simpler homogenization techniques. The older methods use experimental data and compile the behavior into one model [17], which is hard to generalize. As an extension, one can try to find analytical expressions which match these datasets [9, 18] as a way to interpolate between experiments. This is not always very accurate when straying from experimental results. For periodic masonry, however, an analytical expression for the effective elastic stiffness of the unit cell was formulated by Wang et al. using a one step approach [12]. This analytical method works for most simple RVE types, and can be used to calibrate new numerical models. As a more general solution one can use a previously calibrated computational model to calculate the elastic response of the RVE [19, 20]. The main advantages are a very broad and fast applicability, but when the model is not accurately calibrated there is a risk of inaccuracy. The main advantage of a computational approach, as well as an analytical approach, is that one only needs to determine in advance the mechanical properties of the separate elements. This means that it is only necessary to know the material properties of the type of brick and mortar used, as well as the geometry of the system, to formulate a complete model.

The model discussed in this contribution involves using newer scale embedding multiscale techniques [21, 22], a multi-resolution solution [23] where the geometry is divided into parts which are modeled using macroscale techniques and other parts which use microscale techniques, as seen in Figure 3. In this figure the blue microscale geometry is modeled simultaneously with

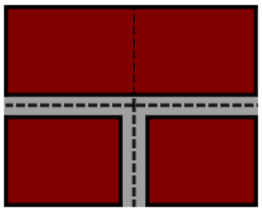

Figure 1: The most probable crack locations in masonry.

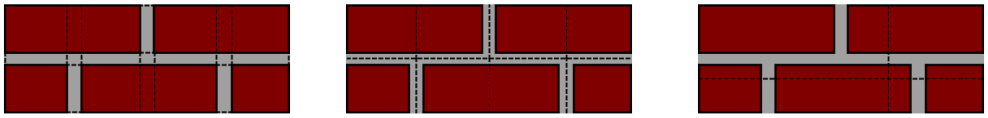

(a) Detailed microscale (b) Simplified microscale (c) Macroscale

Figure 2: Traditional masonry models.

the green macroscale mesh. Depending on the technique used, these parts can be explicitly connected through an extended stiffness matrix and solved simultaneously, or they can be implicitly connected via Lagrange multipliers using domain decomposition techniques leading to multiple smaller stiffness matrices [24, 25, 26, 27]. Both types have their advantages and disadvantages and are useful for different types of modeling.

Most of the work on multiscale modeling has been focused towards scale transition models, in which one uses information from the microscale model to calibrate the macroscale model, a way of achieving homogenization. On the other hand, the concurrent approach can calculate these macroscale parameters during the simulation when needed, leading to a more coupled approach between the micro- and macroscale. The macroscale homogenization in this work is formulated via a concurrent type scale transition model.

Previous studies on this subject were performed by Greco et al. [28, 29] using a model written in COMSOL. These followed earlier work by Heyens et al. [22]. The main novelty in the current work is the focus on improving the computational efficiency on top of achieving a high accuracy, as well as giving a simple real world example showing the broader applicability of the model.

The modeling strategy developed in this work considers two dimensional in-plane unreinforced masonry, consisting in general of a repeating micro-

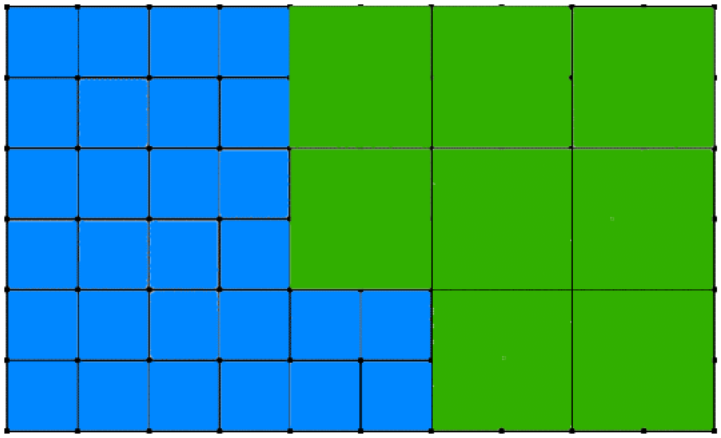

Figure 3: An example of the scale embedding multiscale approach, combining a blue microscale and green macroscale method.

structure, where any force or displacement is applied quasi-statically. Due to a relatively small thickness of the masonry wall, and the negligence of out-of-plane behavior, this work assumes plane stress conditions.

In this contribution, Section 2 will outline the modeling framework necessary for modeling masonry structures using non-linear simplified microscale and linear elastic macroscale methods. This is achieved through the description of the used damage model and the necessary homogenization methods. Further, the domain activation method itself will be outlined and the accompanying computational flowchart is given. In Section 3, three sample systems are described that will be compared using the domain activation method from Section 2 and its underlying microscale method. The focus will be on comparing the necessary accuracy of the methods, as well as their computational efficiencies. There will also be a discussion on the choice of the RVE. The results of this research are then shown, also including results of the influence of the RVE on accuracy and efficiency. Then, in Section 4 one can find the discussion of a simple application: large scale soil subsidence under a blind wall. Finally, Section 5 outlines the conclusions of this work.

2. Modeling framework

In this section the necessary modeling framework is discussed. In short, the model is composed of two stages, the initial macroscale and resulting microscale mesh, connected through an adaptive domain activation procedure.

The macroscale model is chosen to be linear elastic and analytically homogenized while all the non-linear effects are simulated in the microscale mesh. Activation, the replacement of a macroscale element with its underlying microscale geometry, happens based on a critical strain surface that is calculated as the surface where damage first occurs in the RVE. The microscale model is based on previous work by Vandoren et al. [30].

2.1. Damage model

When using non-linear interfaces to represent the weak connections between solid elements, such as in the simplified macro-modeling, one must specify a law which connects the structural response to the introduction of damage in these interfaces. Here we use an isotropic damage model in which the stiffness of the interface is scaled with a factor $1-\omega$ [31],

$$\mathbf{t} = (1-\omega)\mathbf{D}\Delta\mathbf{u}, \tag{1}$$

in which $\mathbf{t}$ are the tractions and $\Delta\mathbf{u}$ the relative displacements along the interface, and $\omega \in [0,1]$ is called the damage factor. Here $\omega = 0$ means the interface element is undamaged with full stiffness, while $\omega = 1$ means full damage and zero remaining stiffness.

The damage scaling is chosen to follow an exponential softening law:

$$\omega = \begin{cases} 0 & \text{if } d_{\max} < d_{\min} \\ 1 - \dfrac{d_{\min}}{d_{\max}} e^{\alpha(1-d_{\max}/d_{\min})} & \text{if } d_{\max} \geq d_{\min} \end{cases}, \tag{2}$$

with $d_{\min} = \sigma_{\mathrm{t}}/K_{\mathrm{n}}$ being the threshold interface jump before damage initialization, $d_{\max}$ the maximum value attained by the equivalent displacement jump d_{eq}, and finally α representing the brittleness of the mortar via

$$\alpha = \left(\frac{G_{\mathrm{c}}}{\sigma_{\mathrm{t}} d_{\min}} - \frac{1}{2} \right)^{-1}. \tag{3}$$

In this formula G_{c} represents the mode I fracture energy of the mortar, and σ_{t} its uniaxial tensile strength. K_{n} is the normal stiffness of the mortar joint.

The Drucker-Prager model [32] defines the equivalent displacement jump as

$$d_{\mathrm{eq}} = \begin{cases} AI + BJ & \text{if } J \geq \dfrac{A-C}{D-B} I \\ CI + DJ & \text{if } J < \dfrac{A-C}{D-B} I \end{cases}, \tag{4}$$

leading to a softening response in tension with a compressive cap. The variables A, B, C, and D, are defined as

$$A = \frac{\sigma_\mathrm{c} - \sigma_\mathrm{t}}{2\sigma_\mathrm{c}}, \tag{5}$$

$$B = \frac{\sqrt{3}}{2}\frac{\sigma_\mathrm{c} + \sigma_\mathrm{t}}{\sigma_\mathrm{c}}, \tag{6}$$

$$C = \frac{(\sigma_b - \sigma_\mathrm{c})\sigma_\mathrm{t}}{\sigma_\mathrm{b}\sigma_\mathrm{c}}, \tag{7}$$

$$D = \frac{\sqrt{3}(2\sigma_\mathrm{b} - \sigma_\mathrm{c})\sigma_\mathrm{t}}{\sigma_\mathrm{b}\sigma_\mathrm{c}}, \tag{8}$$

where σ_c is the uniaxial compressive and σ_b the biaxial compressive strength. Finally, the jump invariants are given by

$$I = (1 + \nu_\mathrm{m})u_\mathrm{s}, \tag{9}$$

$$J = \frac{1}{1 + \nu_\mathrm{m}}\sqrt{\frac{1}{3}u_\mathrm{n}^2(\nu_\mathrm{m}^4 + \nu_\mathrm{m}^3 + \nu_\mathrm{m} + 1) + \frac{1}{4}u_\mathrm{s}^2}, \tag{10}$$

with u_n and u_s being, respectively, the normal and tangential displacement jumps, and ν_m the Poisson's ratio of the mortar joint.Due to the nature of this Drucker-Prager model with the compressive cap, masonry crushing is implicitly modeled in the stress-strain diagram. [1]

The choice to use a damage model is made due to several reasons. The first and most obvious one is because of the relative simplicity over more complicated models such as plasticity based approaches, meaning a more straightforward and predictable response under the considered different loading conditions. Also this simplicity generally makes for a more computationally efficient and robust implementation (e.g. no iterations are needed at integration point level, which is the case in multi-surface plasticity-based materials model). Secondly, for the cases discussed in this work, namely shear and settlement conditions, such damage models can be considered to be sufficiently accurate. A limitation is that in the case of other more involved loading conditions, such as for example a cyclic loading, one will need to consider other more advanced material models to gain an accurate representation. [30].

2.2. Domain activation method

2.2.1. Micro-macro connection

Crucial to any finite element model is the way connections between elements are handled. Traditional connections like micro-micro and macro-

macro are trivial, with both edges containing only matching nodes. On the other hand, connecting a macroscale element to its neighboring microscale elements is less simple. This is due to the non-matching nodes: the macroscale element will usually have a smaller amount of nodes, and for a four-node macroscale element only the two edge nodes can be directly attached.

One way to solve this is to connect the two domains using a Lagrange multiplier approach [33, 27, 34]. This is necessary when one wants to use domain decomposition methods for tackling the multiscale problem, but could also be applied outside of domain decomposition. This increases computational performance when combined with domain decomposition. The reason it has a high efficiency is because domain decomposition splits the normally very large stiffness matrix into multiple smaller ones, one for each domain, allowing multi-core solvers to be easily implemented. A second possible solution is to use a direct connection method, whereby one applies a hard connection between the outer two corresponding nodes of the microscale and the multiscale regions and leaves the inner nodes of the microscale model unbound, as seen in Figure 4 where only the white nodes are connected. In this case, instead of creating new smaller stiffness matrices connected via Lagrange multipliers, the main stiffness matrix is simply expanded to include the new degrees of freedom. The main advantages are its accuracy (due to added robustness and a possibly tighter connection) and a high stability, but performance might lower in comparison due to the added equations that need to be solved. This method can be used in most cases because a macroscale element will be refined before being subjected to a high deformation, after which the full micro-micro connection is made. Due to its stability and straightforwardness the direct connection method is used in this work.

This method, similar to other methods where only a main stiffness matrix is considered, can also be seen as a remeshing method. In this case the local low resolution mesh at the macroscale will get replaced by a more complex higher resolution mesh of the underlying microscale elements. The lack of a connection between the inner microscale nodes and the adjacent macroscale element indicates an incompatibility between these elements nodes, which means there can be a local disconnection between elements. This is not expected to be a problem since if the adjacent microscale element is strained to reach such a disconnected state, the macroscale region will be under similar strain and is expected to be refined anyway, solving the local disconnection.

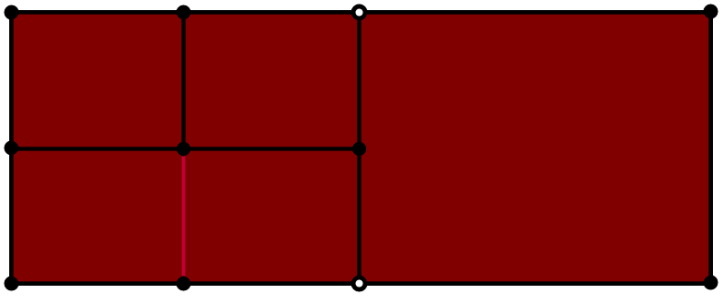

Figure 4: The connections between a microscale (left) and a macroscale (right) region.

2.2.2. Refinement criteria

A crucial part of using a scale embedding multiscale model comes from the right choice of refinement criteria [27, 23]. Refining the mesh too early means most of the performance gain is lost, but refining too late leads to the use of simple macroscale elements when damage effects should have been included. One possibility, which is used in the present research, is the use of a strain surface, where one defines the maximum strains a macro-element should reach before inducing refinement. Finally, these results will be interpolated between different loading conditions, leading to a strain surface upon which one expects relevant damage to occur in the macro-element. Once such an element reaches this threshold it is refined into its accompanying microscale geometry.

There are a few possibilities to calculate this strain surface, and the classical method involves the use of experimental [35, 36, 37] studies. The problem is, again, that these methods are not easily extended towards different geometries or radically different material properties. Thus, an alternative is the use of a computational method where one applies a multitude of different loading conditions on the chosen microscale RVE and records for each case the strain present in the model at a chosen damage criterion. This damage criterion can be chosen to be as flexible or restrictive as necessary, and represents the aforementioned balance between performance and accuracy.

In this case one chooses the criterion to be the appearance of any nonlinearity in the microscale RVE, which in practice means that the damage value ω is nonzero for any interface element in the RVE.

Finally, one can calculate the strain surface for the chosen RVE, by varying two angles θ_1 and θ_2, defined in a way such that the normal and shear

strains acting upon the element are given by

$$\epsilon_x = \beta \sin(\theta_2) \cos(\theta_1), \tag{11}$$
$$\epsilon_y = \beta \sin(\theta_2) \sin(\theta_1), \tag{12}$$
$$\epsilon_{xy} = \beta \cos(\theta_2), \tag{13}$$

as shown in Figure 5, where the blue represents a fixed boundary condition and green the applied displacement .

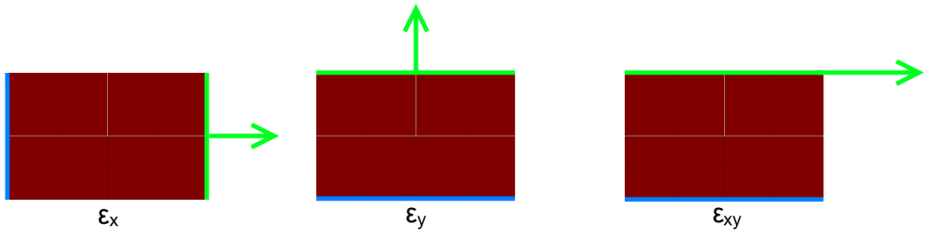

Figure 5: The strains as applied to the RVE.

In these equations the value β is the strain factor, and for every combination of θ_1 and θ_2 a factor $\beta_c(\theta_1, \theta_2)$ is determined as the value of β for which damage starts to occur in the elements. Due to symmetry the range of the angles is $\theta_1 \in [0, 2\pi]$ and $\theta_2 \in [0, \pi/2]$. One determines the critical strain surface by finding a value of β_c for every combination of θ_1 and θ_2, which in practice is done by iterating over both variables and interpolating the results to approximate a continuous solution.

To find the location of a macroscale element compared to the critical strain surface one measures the three macrostrains mentioned above and from these calculate the two angles via the derived formulas

$$\theta_1 = \tan^{-1}\left(\frac{\epsilon_x}{\epsilon_y}\right), \tag{14}$$
$$\theta_2 = \tan^{-1}\left(\sin(\theta_1)\frac{\epsilon_{xy}}{\epsilon_y}\right). \tag{15}$$

From these calculated angles the corresponding critical strain factor β_c can be compared to the measured one, and if $\beta > \beta_c$ the element is scheduled for refinement. For example, choosing $\theta_2 = \pi/2$ and varying θ_1 from 0 to 2π one gets a system in which no shear force is applied, only normal forces,

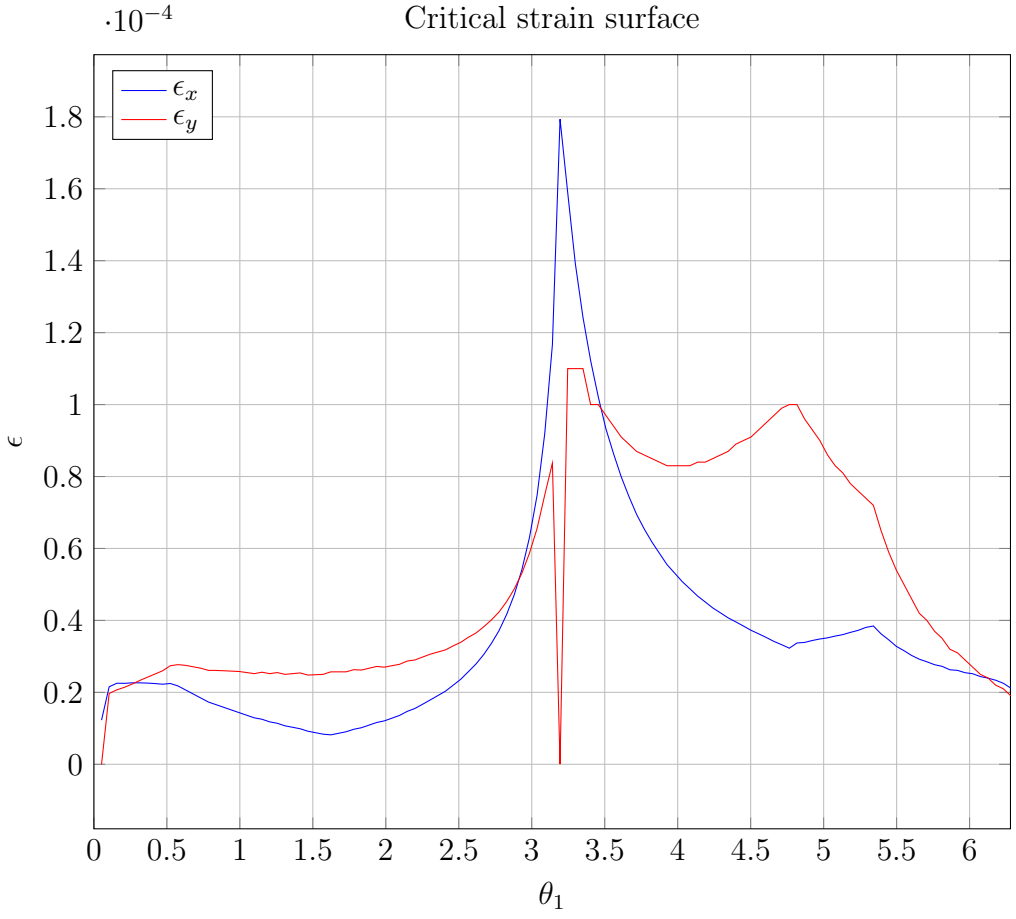

Figure 6: Critical strain surface for $\theta_2 = \pi/2$.

following formulas (11)-(13). For this specific range of angles the horizontal and vertical critical strains ϵ_x and ϵ_y are shown in Figure 6 in function of the angle θ_1. The results show that during compression in both the horizontal and vertical dimensions the critical strain is the largest, while when at least one of the sides is in tension the critical strain is a lot lower, with masonry being stronger in compression than in tension.

Performance balancing of the framework is possible by changing two parameters before determining the strain surface: a scaling factor c_s which enlarges or shrinks the effective calculated strain surface β_eff as $\beta_\mathrm{eff} = c_\mathrm{s}\beta_\mathrm{c}$, or by choosing a non-zero allowed damage in the RVE. These two parameters are computational parameters, not material ones, and only exist to balance

performance. In this work the influence of the parameter c_s is studied to obtain more insight into the accuracy/efficiency balancing.

An alternative strategy is the use of non-adaptive elements where the location of damage initialization is determined in advance[38]. An advantage is that if these locations are well known the inherent danger of the use of adaptive elements is minimized. In this case using adaptive elements means that, if missing an important refinement somewhere in the model evolution, there exists a possibility of the final case being inaccurate. An important issue is finding these nonlinear locations without performing a full microscale simulation, meaning that the more traditional methods are rendered useless. Instead one can use for example a NURBS-based procedure[39] wherein a very fast genetic algorithm is used to predict these zones of failure, and then use a non-adaptive multiscale model to model the system.

2.3. Homogenization techniques

For large structures it becomes helpful to remove the inherent element size limit imposed on micro- and mesoscale methods by incorporating macroscopic elements. These macroscopic elements can encompass an unlimited amount of the underlying material, a big contrast to the smaller scale alternatives. The use of these elements, however, means that one needs to find a way to condense the complex behavior of the underlying RVE into one continuum element. This is done through homogenization, combining constituent material parameters and geometry into an encompassing constitutive law that tries to mimic the RVE's accurate reactions to external forces or displacements [21, 40, 41].

An example of a recent analytical method by Wang et al. [12] is given here, with the results summarized in brief. This method is used when calculating the RVE elastic stiffness in the rest of this work. First, one defines $\mathbf{K}_B$ and $\mathbf{K}_M$ to be the elastic stiffness matrices of the brick and mortar included in the RVE. f_B is the volume fraction of brick inside the RVE, with a and b the horizontal and vertical dimensions of the brick, and L and H the horizontal and vertical dimensions of the RVE. To calculate the elastic stiffness we need to define the Eshelby tensor as the summation of an infinite Fourier series

$$\mathbf{S}^{\Omega}_{ijmn} = \sum_{\xi \in \Lambda} f_B g_0(\xi) g_0(-\xi) \mathbf{g}_{ijmn}(\xi), \tag{16}$$

with Λ the set on which the summation is made on:

$$\Lambda = \left\{ \xi = \xi_1 e_1 + \xi_2 e_2 \mid \xi_1 = \frac{n_1 \pi}{L}, \xi_2 = \frac{n_2 \pi}{H}; n_1, n_2 = 0, \pm 1, \pm 2...; n_1^2 + n_2^2 \neq 0 \right\}. \tag{17}$$

$g_0(\xi)$ is the function of bond geometry, which for a running bond is defined as

$$\begin{aligned} g_0(\xi) = \frac{1}{2ab} \frac{1}{\xi_1 \xi_2} [&\sin(\xi_1 b) \sin(\xi_2 a) \\ &+ (\sin(\xi_1 L) - \sin(\xi_1 (L-b))] \cdot [\sin(\xi_2 H) - \sin(\xi_2 (H-a))]. \end{aligned} \tag{18}$$

Finally, if one assumes an isotropic brick and mortar behavior, $\mathbf{g}_{\mathrm{ijmn}}(\xi)$ is defined as

$$\begin{aligned} \mathbf{g}_{\mathrm{ijmn}}(\xi) = \frac{1}{2\xi^2} &[\xi_{\mathrm{j}}(\delta_{\mathrm{in}} \xi_{\mathrm{m}} + \delta_{\mathrm{im}} \xi_{\mathrm{n}}) + \xi_{\mathrm{i}}(\delta_{\mathrm{jn}} \xi_{\mathrm{m}} + \delta_{\mathrm{jm}} \xi_{\mathrm{n}})] \\ &- \frac{1}{1-\nu} \frac{\xi_{\mathrm{i}} \xi_{\mathrm{j}} \xi_{\mathrm{m}} \xi_{\mathrm{n}}}{\xi^4} + \frac{\nu}{1-\nu} \frac{\xi_{\mathrm{i}} \xi_{\mathrm{j}}}{\xi^2} \delta_{\mathrm{mn}}. \end{aligned} \tag{19}$$

To obtain the effective elastic stiffness of the RVE $\mathbf{K}_{\mathrm{h}}$ one uses the expression

$$\mathbf{K}_{\mathrm{h}} = \mathbf{K}_{\mathrm{M}} : [\mathbf{1} - f_{\mathrm{B}} (\mathbf{A}_{\mathrm{B}} - \mathbf{S}_{\mathrm{B}})^{-1}], \tag{20}$$

with

$$\mathbf{A}_{\mathrm{B}} = (\mathbf{K}_{\mathrm{M}} - \mathbf{K}_{\mathrm{B}})^{-1} : \mathbf{K}_{\mathrm{M}} \tag{21}$$

and $\mathbf{S}_{\mathrm{B}}$ the relevant Eschelby tensor.

3. Numerical examples

In this section three numerical examples are presented, a medium-sized and two large-sized walls with opening, for which the numerical results of the presented scale embedded multiscale model will be compared to a reference microscale model. The model will be tested on these three differently sized walls to check a consistent accuracy across multiple systems, but also to study the influence of wall size on the efficiency of the multiscale over the microscale method.

3.1. Geometric and material parameters

We use three different setups to test the developed multiscale model, all 2D masonry walls with an opening near the center. The first is a smaller sized wall, shown in Figure 7. The second wall is a larger version of this wall, shown in Figure 8. Finally the last example is even larger vertically and is shown in Figure 9. The geometrical properties of all these walls are shown in Table 1. All of these walls will be fixed on the bottom and top, with a horizontal displacement to the right applied to the top bricks. In the figures the fixed boundary conditions are represented in blue, and the applied displacements in green. It starts from an undamaged rest state, from which displacement increments will be applied until failure of the wall occurs.

Table 1: Geometric properties of the walls.

	Wall 1	Wall 2	Wall 3
Width (m)	1.10	2.64	3.96
Height (m)	1.26	1.68	3.36
Depth (m)	0.1	0.1	0.1
Brick width (m)	0.22	0.22	0.22
Brick height (m)	0.07	0.07	0.07
Mortar thickness (m)	0.01	0.01	0.01

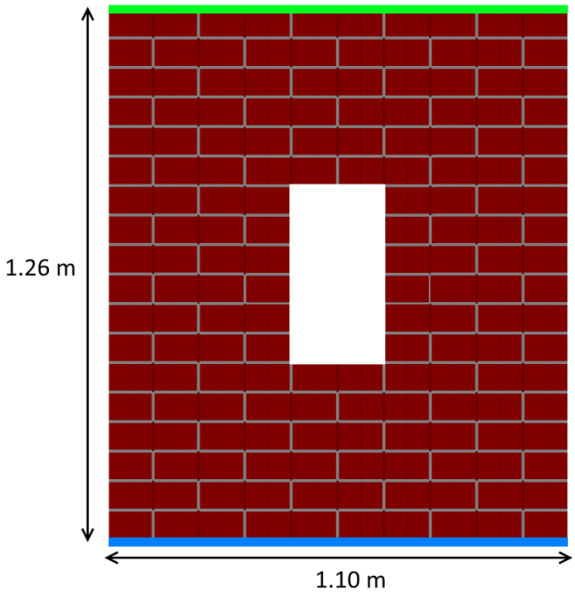

Figure 7: The first wall setup.

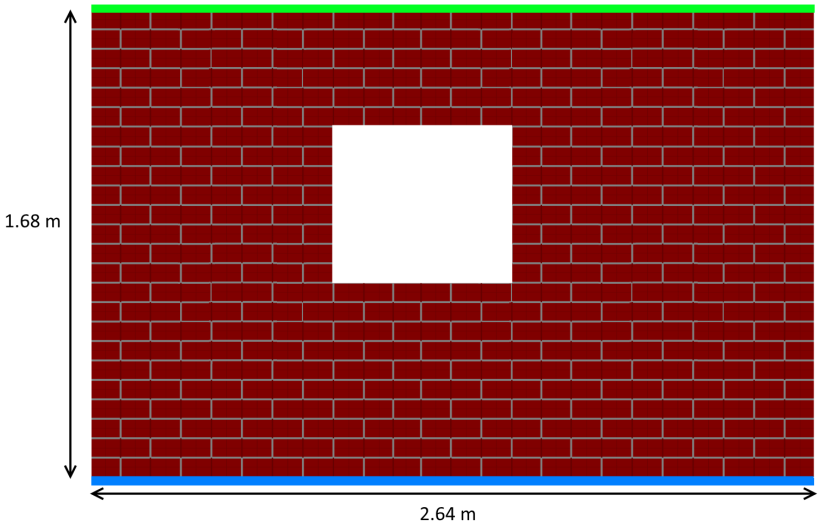

Figure 8: The second wall setup.

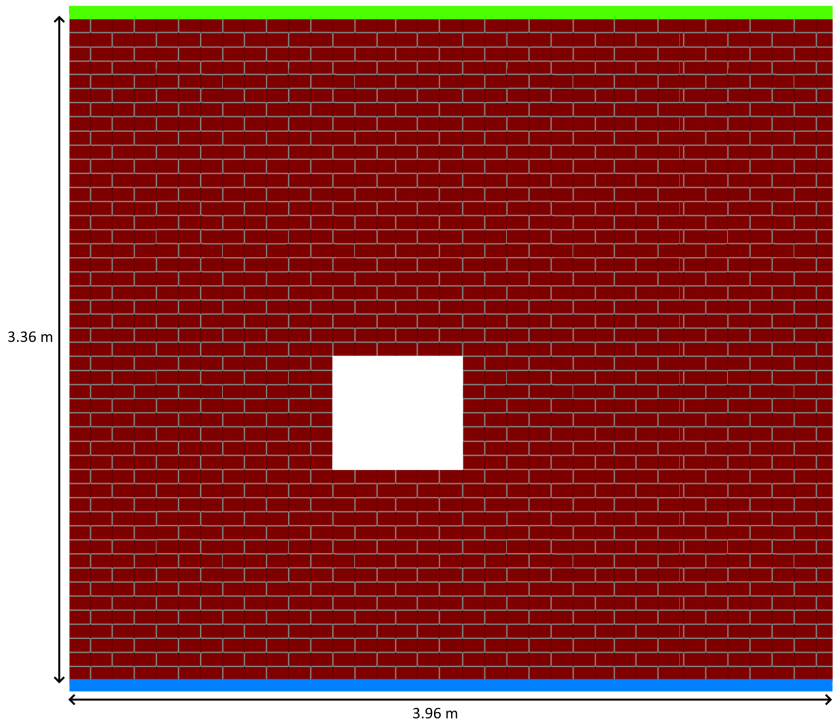

Figure 9: The third wall setup.

The material properties are given in Table 2, chosen to be representative of a commonly used brick and mortar combination [42].

Table 2: Physical properties.

Material	Brick	Mortar
Young modulus (GPa)	16	8
Poisson's ratio	0.15	0.15
Gf_{I} (N/m)	1000	18
σ_{t} (kN/m^2)	1000	250
σ_{c} (kN/m^2)	100,000	11,000
σ_{b} (kN/m^2)	120,000	12,500

3.2. Choice of the RVE

To accommodate the multiscale modeling, the system geometries need to be able to be split up into macroscale elements, mimicking the behavior of the underlying RVE. The choice of which RVE to use is important: choosing a small RVE makes the initial model slightly slower, due to the larger number of macroscale elements, but in the end leads to a possibly more efficient model, depending on the occurring nonlinear effects. This is shown in Figure 10 where in the first step, when no damage has occurred yet and the system is still fully linear, the amount of elements for a small RVE is larger than for a large RVE. However, when damage starts to occur and the system undergoes damage, the ratio between microscale and macroscale area swings in favor of the smaller RVE model. To conclude, when nonlinearities are present, a smaller RVE is generally the better choice.

The RVE given in Figure 11 is the smallest macroscopic building block possible, which is called the Unit Cell (UC). It consists of two half bricks, and one complete brick. This choice of RVE is used throughout this research. In addition, the initial number of elements in the macroscale as well as the number of elements in the microscale geometry, which is also the maximum number of elements in the multiscale method, is shown in Table 3.

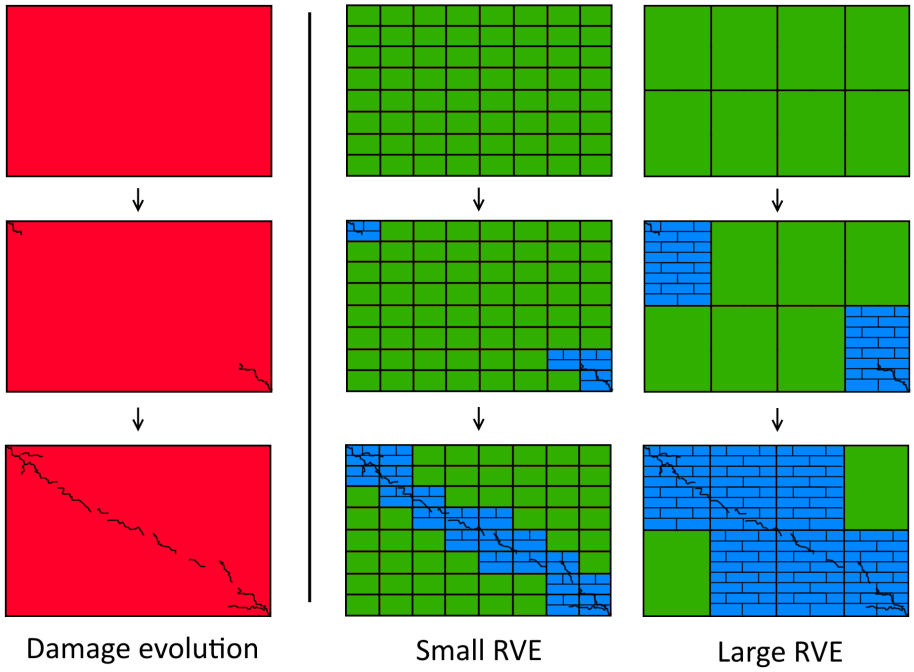

Figure 10: Influence of the RVE size on refinement.

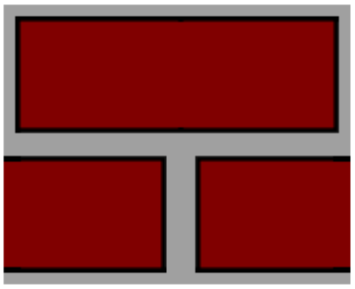

Figure 11: The chosen RVE.

Table 3: The number of elements.

	Wall 1	Wall 2	Wall 3
Macroscale	47	132	420
Microscale	1,128	3,168	10,080

3.3. Results

To check the validity of the proposed multiscale model, the computational results will be compared to their corresponding microscale model. Properly comparing the microscale model and the corresponding multiscale model means that one needs to define some comparison criteria. Firstly, accuracy needs to be tested. This can be done by looking at both the force-displacement curve, especially the critical force and displacement, and the crack evolution. If the multiscale model is indeed accurate, one can compare efficiencies by looking at the model run times.

At first, both the microscale and multiscale model will be in their undeformed and undamaged states, which is shown in Figures 7, 8, and 9. Following this, small displacement control increments are applied and solved iteratively using a Newton-Raphson method. In the multiscale model, during every incremental step the remaining macroscale elements are checked, and if they exceed the calculated strain surface in Figure 6 they are marked. At the end of every incremental step the marked elements are removed and replaced by their underlying RVE. This is repeated until failure is reached or the simulation is halted. This is shown in the the flowchart in Figure 12.

3.3.1. Accuracy

The most important quantities to compare when checking the accuracy between both models are the critical force and critical displacement of the system, as well as the overall progression of the force-displacement curve. A second criterion is looking at the formation and propagation of the crack pattern itself.

First we compare the results of the microscale model to the reference multiscale model, the force-displacement curves are shown in Figure 13 for the first wall, in Figure 14 for the second wall, and finally in Figure 15 for the final wall. The crack pattern development (as well as that of the scale refinement pattern) is shown in respectively Figures 16 and 17 for wall 1, Figures 18 and 19 for wall 2, and Figures 20 and 21 for wall 3. In these figures, the range of damage in the mortar interfaces is visually represented from the value zero, no damage, in white to one, no remaining stiffness, in black. One can see that, as the applied displacement increases, more macroscale elements get refined into their underlying microscale elements and the evolution of damage occurs.

Looking at these results one can conclude that both the force-displacement and the crack propagation up to the peak load is very comparable in both

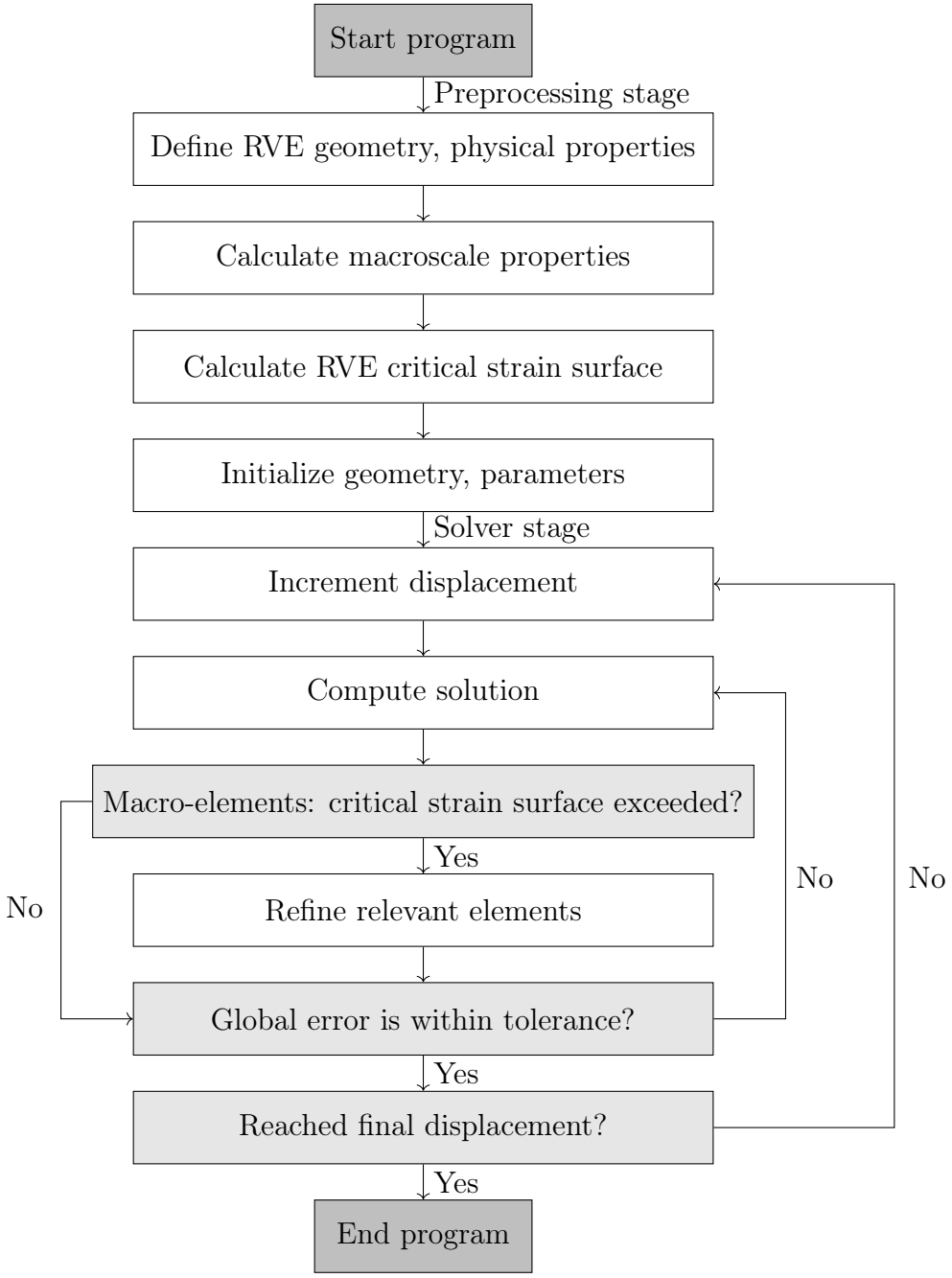

Figure 12: Computational flowchart used in the developed multiscale model.

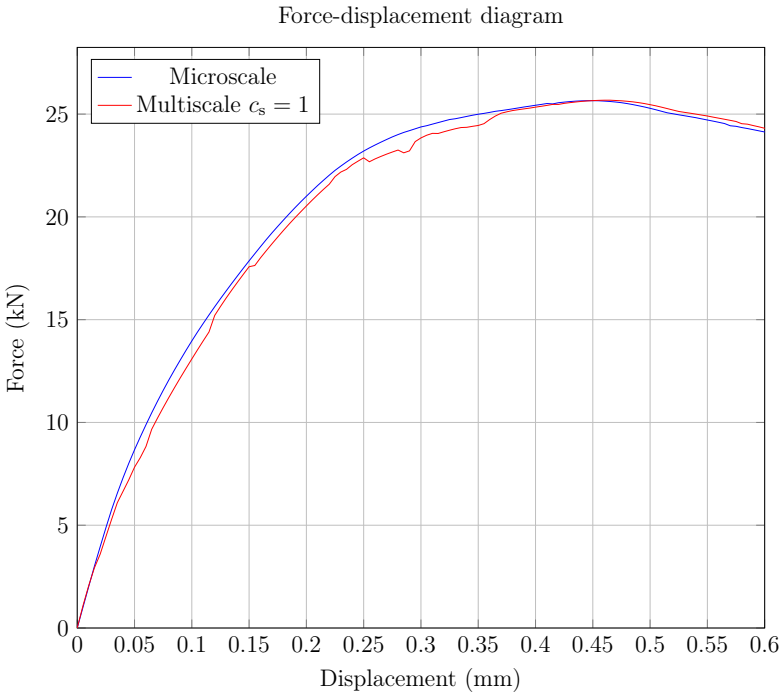

Figure 13: Force-displacement curve of wall 1.

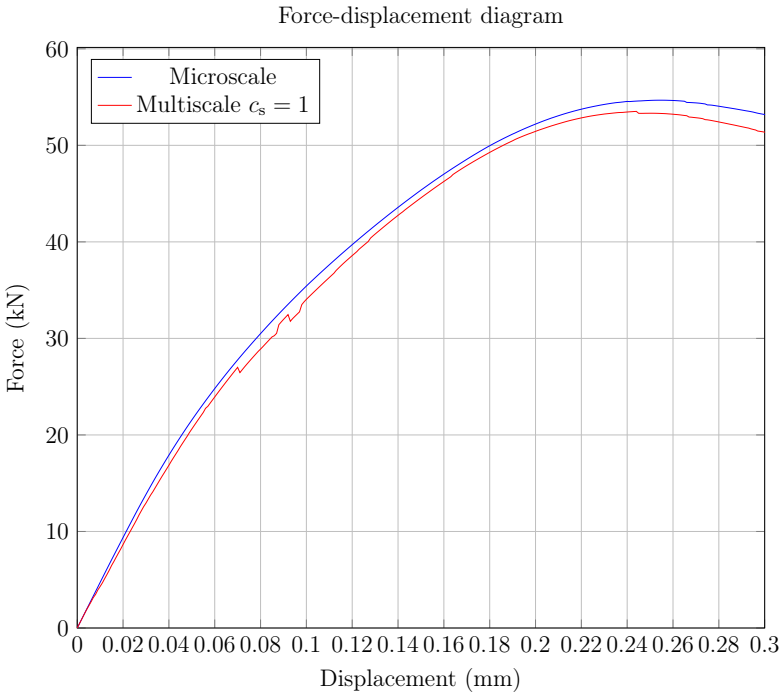

Figure 14: Force-displacement curve of wall 2.

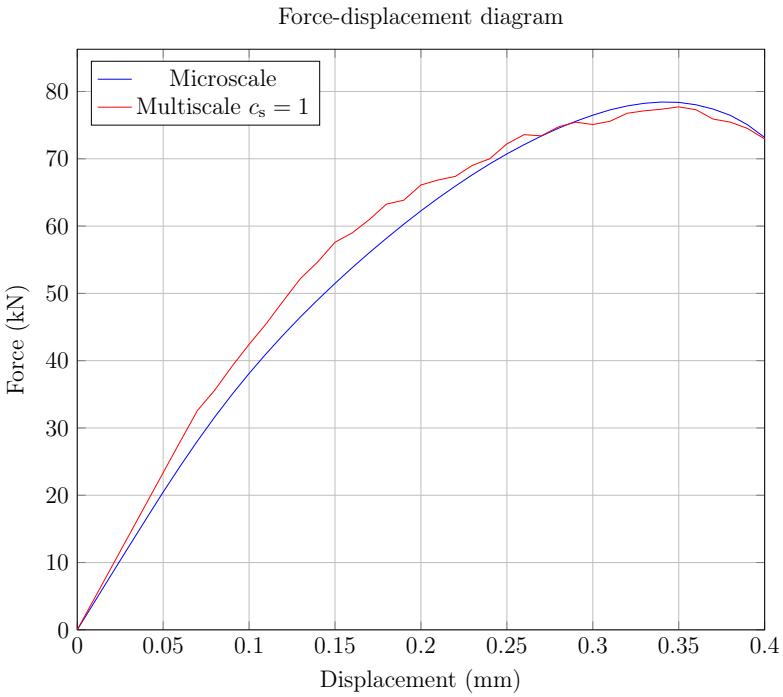

Figure 15: Force-displacement curve of wall 3.

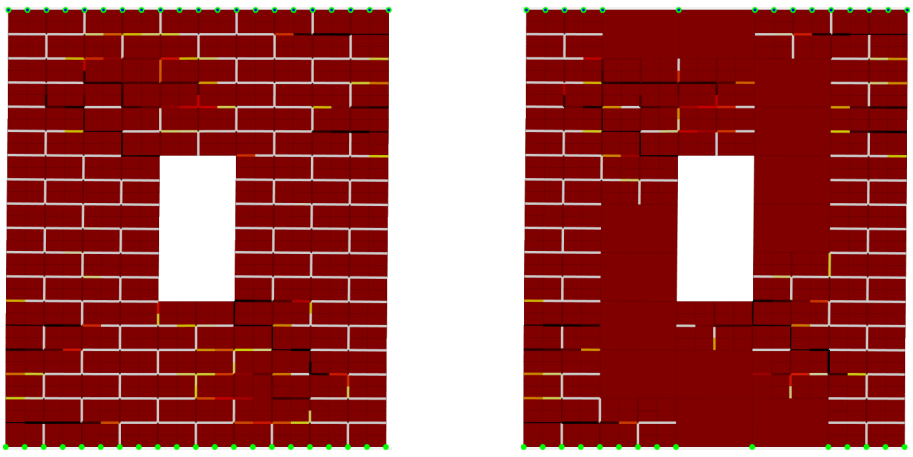

(a) Microscale (b) Multiscale $c_s = 1$

Figure 16: Crack pattern of wall 1 at $d = 0.2$ mm.

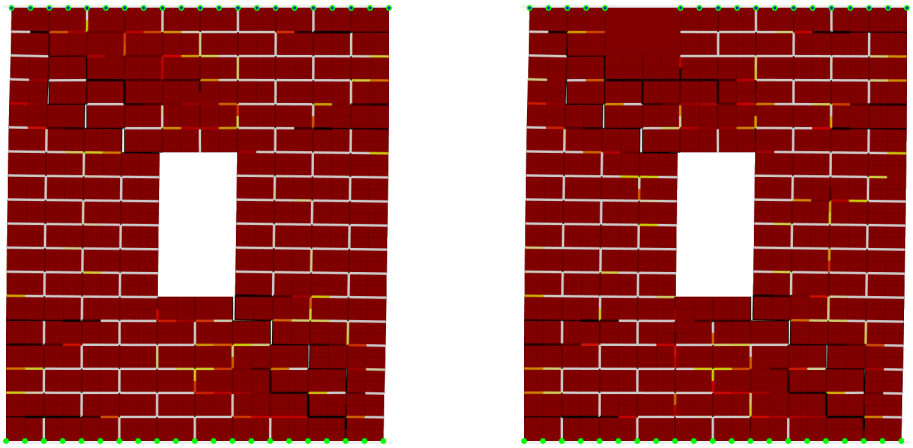

(a) Microscale (b) Multiscale $c_s = 1$

Figure 17: Crack pattern of wall 1 at $d = 0.4$ mm.

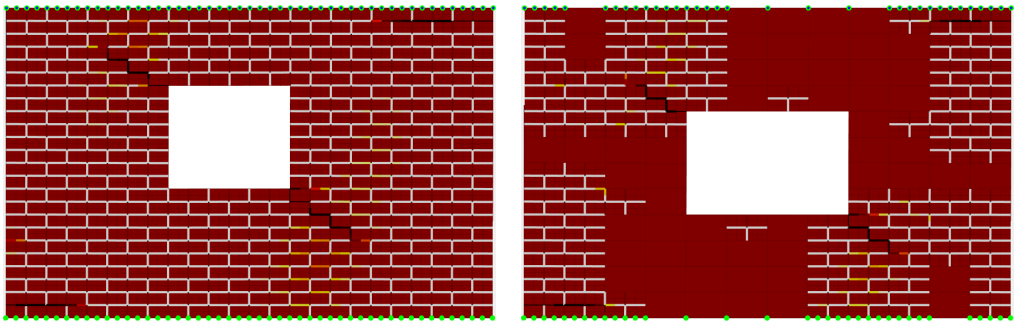

(a) Microscale (b) Multiscale $c_s = 1$

Figure 18: Crack pattern of wall 2 at $d = 0.1$ mm.

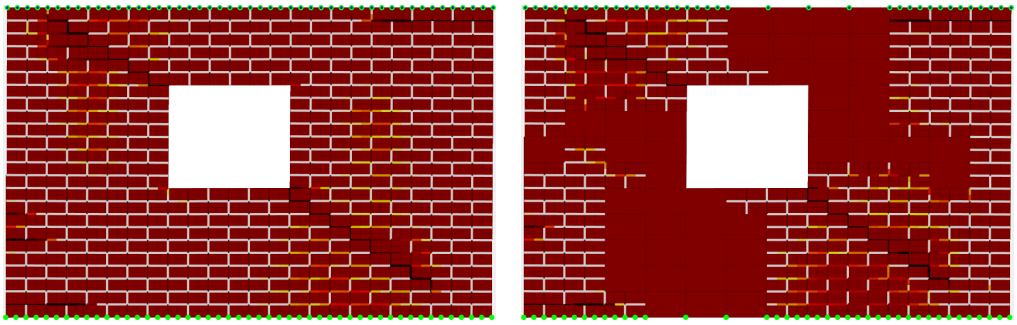

(a) Microscale (b) Multiscale $c_s = 1$

Figure 19: Crack pattern of wall 2 at $d = 0.2$ mm.

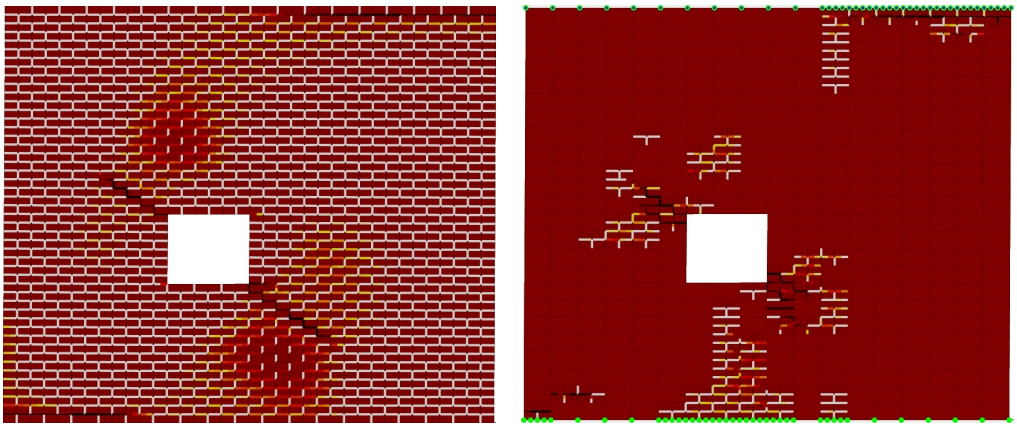

(a) Microscale (b) Multiscale $c_s = 1$

Figure 20: Crack pattern of wall 3 at $d = 0.175$ mm.

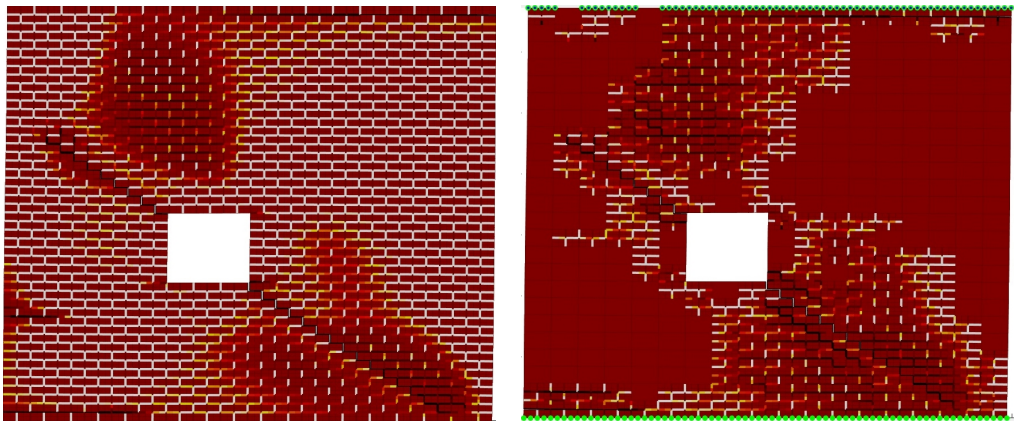

(a) Microscale (b) Multiscale $c_s = 1$

Figure 21: Crack pattern of wall 3 at $d = 0.35$ mm.

models, and thus sufficient accuracy of the reference multiscale model with respect to the microscale model is shown.

3.3.2. Efficiency

The main novelty of the proposed method is the increase in computational efficiency, which will be discussed here. For this, the efficiencies of the microscale and multiscale models have be compared. For this purpose the total runtimes of wall 1 for both models are given in Figure 22, with detailed results given in Table 4. It should be noted that all the simulations were done using MATLAB R2018a under Windows 8.1 on an Intel I5 dual core CPU at a clock speed of 2.60 GHz. It can be seen that the runtime of the multiscale model is $\approx 64\%$ that of the microscale model for the simulation to reach the critical displacement, the displacement at the maximal force. This increase is notable, though not groundbreaking. Looking at smaller applied displacements a larger difference is seen, with the multiscale model reaching half the critical displacement at only $\approx 41\%$ runtime than that of the microscale model.

Table 4: Wall 1 efficiency comparison.

Displacement (% of failure)	Runtime Microscale (s)	Runtime Multiscale (s)	Relative cost (%)
25	337	121	36
50	597	244	41
100	1,108	706	64

In Figure 23 the runtimes of wall 2 are compared, with more detailed results in Table 5. One can see that the difference between both models are greater for this large wall than for the previous smaller one. At the critical displacement, the runtime of the multiscale model is only ≈ 35 %, with a runtime of 5,240 s for the multiscale and 14,910 s for the microscale model. Also in this example, as with the smaller scale wall, it's clear that the largest efficiency gains are at the lower displacement side. At half the critical displacement, the multiscale method has a runtime of only $\approx 25\%$ of the microscale method.

Table 5: Wall 2 efficiency comparison.

Displacement (% of failure)	Runtime Microscale (s)	Runtime Multiscale (s)	Relative cost (%)
25	4,300	687	16
50	7,920	2,030	25
100	14,910	5,240	35

Finally for the largest wall a comparison for the runtimes is shown in Figure 24, and with the detailed results in Table 6. Here again the perfor-

mance increase has improved in comparison to the smaller walls, with at the critical displacement the runtime of the multiscale model being only 17% that of the microscale model. Thus it can be noted that the trend seems to indicate a bigger performance increase in larger-scale walls. The reason for this preference for larger structures can be seen by comparing Figure 16 to 21, where the largest shown displacements for all walls are close to the point of failure. In the first wall most of the macroscale elements have been refined even at a smaller displacement due to a larger relative damage spreading. On the other hand, in the larger second and third walls the damage remains relatively localized to the corners of the opening and the wall itself. From this it can be seen that this embedded multiscale method is more suited for larger systems with more localized nonlinearities, at least in terms of gained computational efficiency. Also, the reason a higher relative efficiency gain occurs closer to the start of the simulation, is because the more nonlinearities occur the more macroscale elements get refined, increasing the total number of elements.

Table 6: Wall 3 efficiency comparison.

Displacement (% of failure)	Runtime Microscale (s)	Runtime Multiscale (s)	Relative cost (%)
25	8,750	83	0.1
50	17,590	610	3.6
100	38,940	6,640	17

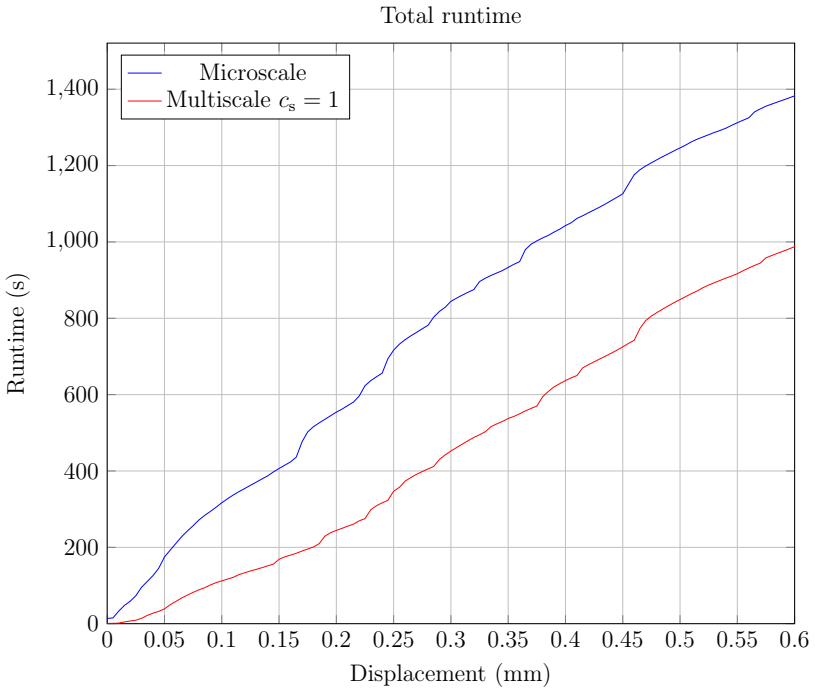

Figure 22: Runtimes of wall 1.

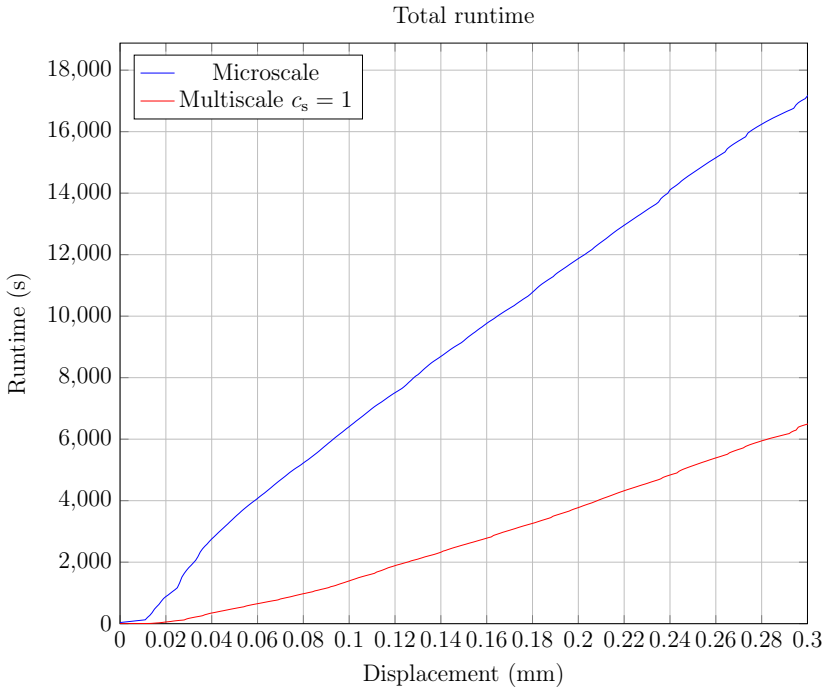

Figure 23: Runtimes of wall 2.

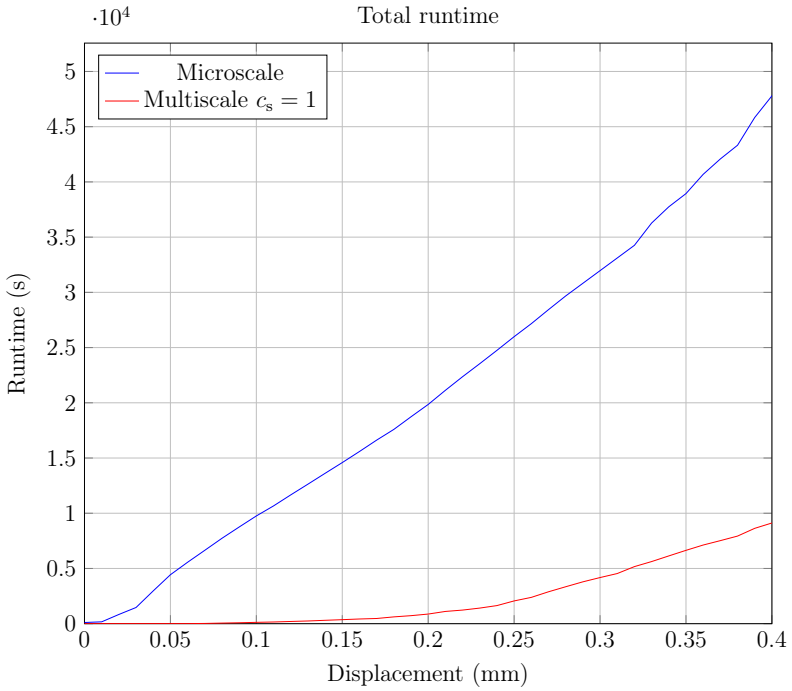

Figure 24: Runtimes of wall 3.

3.3.3. Influence of c_s

In Section 2.2 the scaling parameter c_s was introduced, a factor by which the critical strain surface is enlarged. Choosing c_s larger than unity denotes a larger critical strain surface and thus a postponed refinement. This means that there is loss of accuracy due to damage already being able to occur in unrefined linear elastic macroscale elements, but also an increase in the computational efficiency. On the other hand, a value c_s smaller than unity forces earlier refinement, thus leading to possibly increased accuracy but a lower computational efficiency. Here a few different values are shown and discussed for the second wall, with c_s ranging from unity (the previously used reference model) up until the accuracy loss is deemed unacceptable, which occurs at around $c_s = 1.6$. In Figure 25 the force-displacement curves of the wall are shown for multiple values of c_s and compared to the microscale curve. In Figure 26 the total runtimes are compared as well. One can see that for the force-displacement diagram the results ranging from $c_s = 1$ until $c_s = 1.4$ are still very accurate. When $c_s \geq 1.6$, however, the results seem to diverge. For the runtime comparison one finds that, as predicted, a higher value of c_s indicates a lower total runtime.

The reason for the deviation of the force-displacement curves at high c_s values can be seen in the crack propagation behavior. This is shown in Figure 29, where a comparison is made between the wall at a displacement of 0.2 mm for the multiscale models at $c_s = 1.4$ and $c_s = 1.5$. It is seen that in these cases the cracking pattern is different in both models, caused by late macroscale refinement in the top left and bottom right corners due to the high scaling parameter, which has influenced the force-displacement curves and making the high c_s model more inaccurate.

For wall 3 it is interesting to look at the difference between the models at $c_s = 0.75$ and 1.25, seeing their close agreement in the force-displacement curves but their large separation in computational efficiency. The state of the walls at the critical displacement $d = 0.35$ mm is shown in Figure 30. In this comparison it can be seen that the model using the lower value of $c_s = 0.75$ decides to refine a larger portion of the initial macroscale mesh, leading to a more accurate damage distribution. However, in the $c_s = 1.25$ model the main crack path remains the same despite a lower resolution in the other parts of the model, leading to an almost equally accurate but way more efficient simulation.

To conclude the discussion on the influence of the scaling parameter c_s,

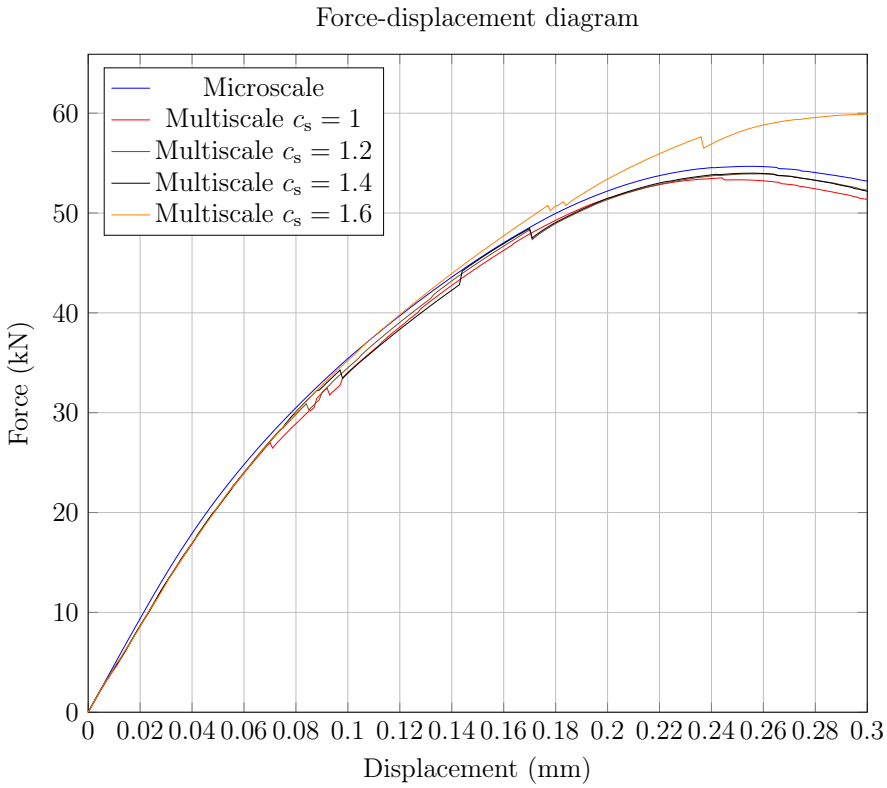

Figure 25: Force-displacement curves of wall 2 at different values c_s.

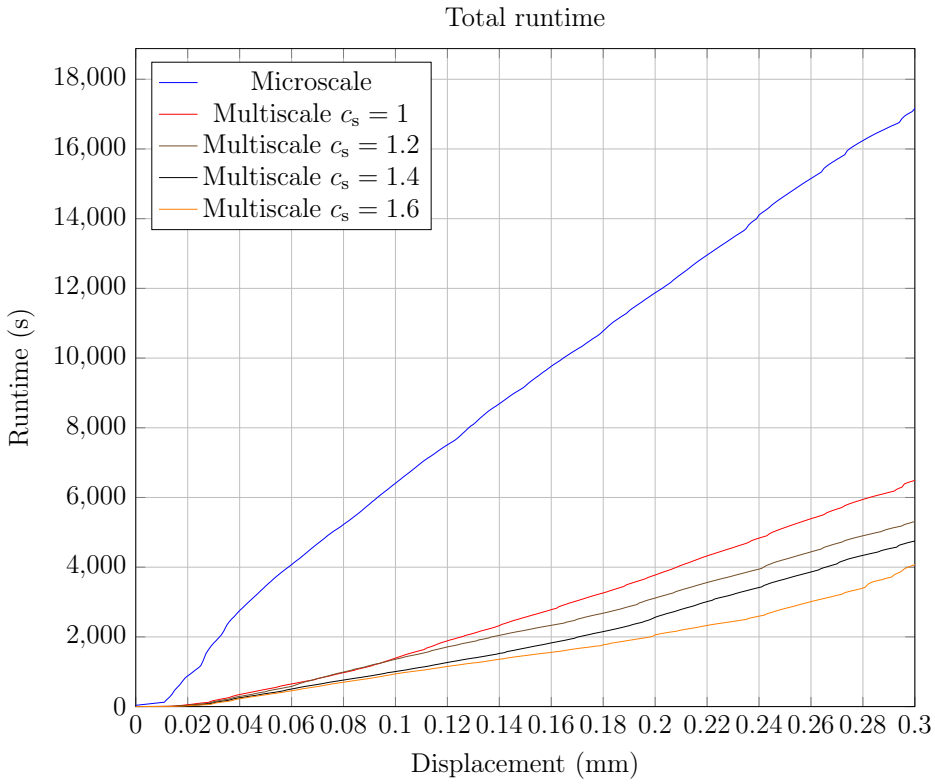

Figure 26: Runtimes of wall 2 at different values c_s.

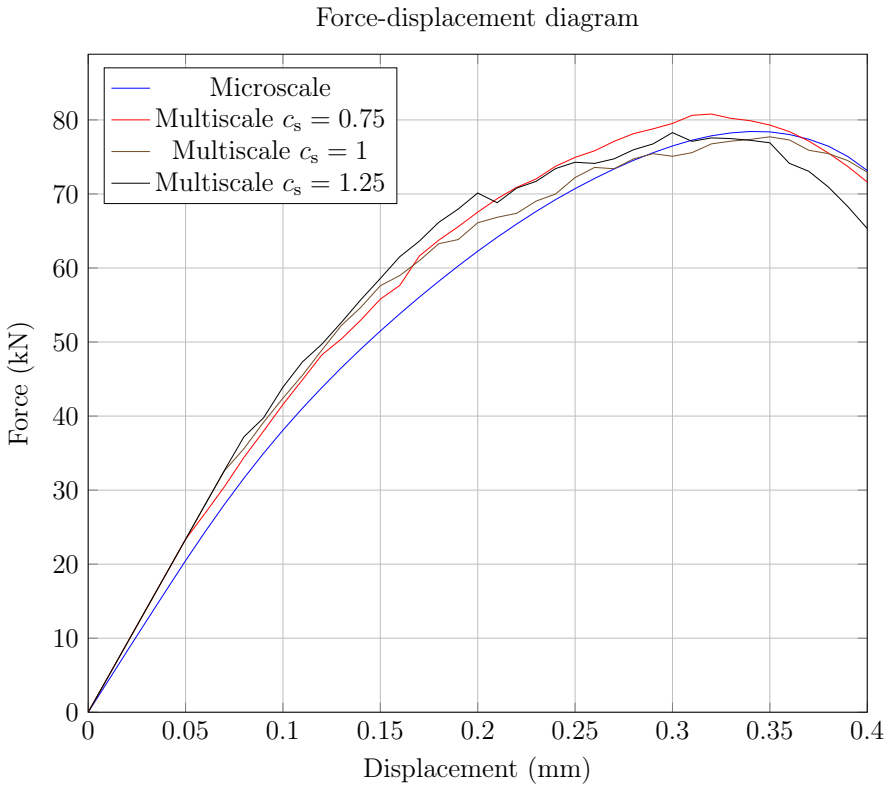

Figure 27: Force-displacement curves of wall 3 at different values c_s.

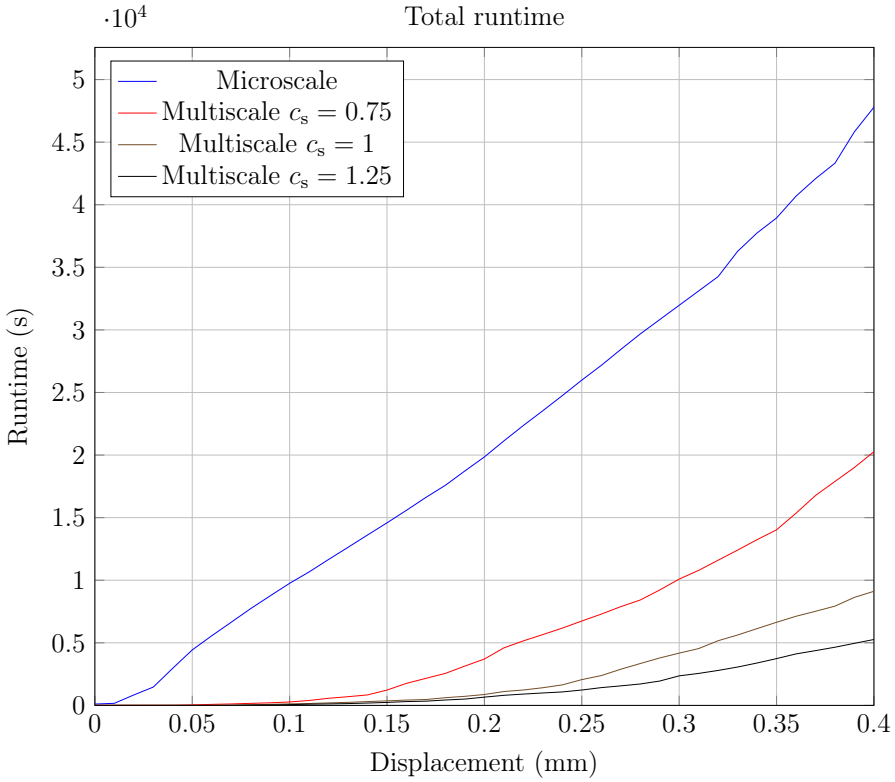

Figure 28: Runtimes of wall 3 at different values c_s.

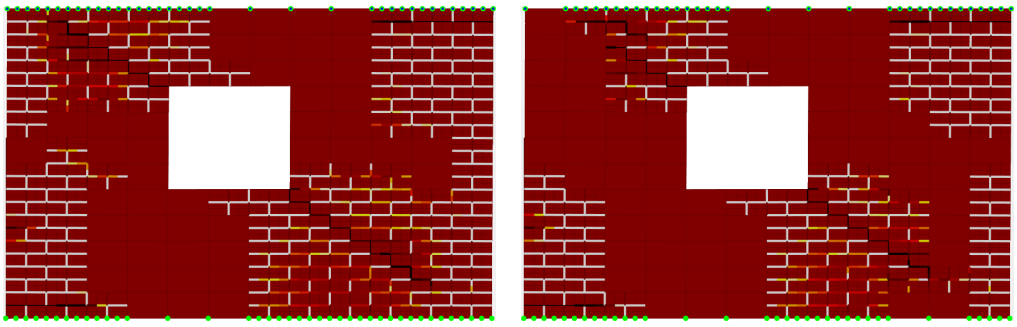

(a) $c_s = 1.4$ (b) $c_s = 1.5$

Figure 29: Multiscale crack pattern of wall 2 at $d = 0.2$ mm.

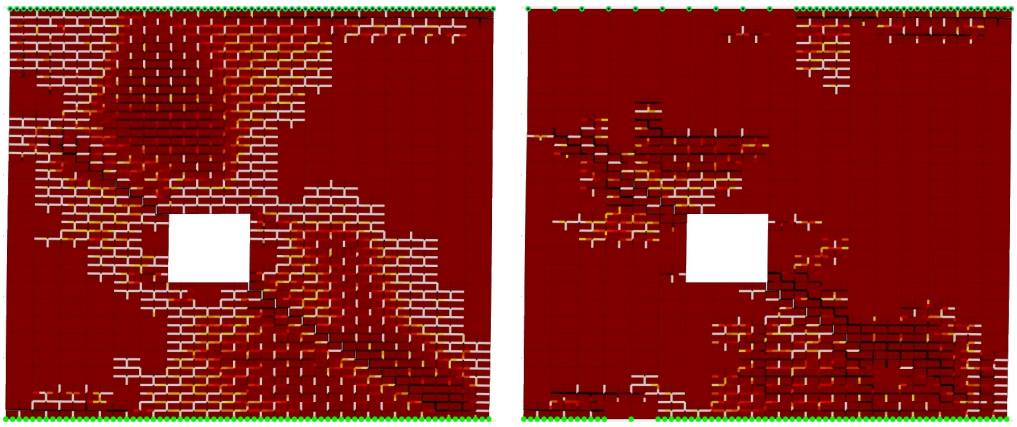

(a) $c_s = 0.75$ (b) $c_s = 1.25$

Figure 30: Multiscale crack pattern of wall 3 at $d = 0.35$ mm.

in Figures 25 and 26 for the second and Figures 27 and 28 for the third wall, one can see that there is indeed a trade off between computational accuracy and efficiency. Here a higher value for c_s results in a more efficient but less accurate result. More so, it is difficult to define a good balance when choosing a value greater than unity, because this will be different depending on the purpose of the research and the system involved. If one only needs to find the ultimate force the wall can withstand, even the factor $c_s = 1.4$ gives a good idea for the second wall, while reaching an efficiency that is about 130% higher than the $c_s = 1$ model. However, when one requires certainty about obtaining an accurately matching force-displacement curve, one needs to choose a factor $c_s \leq 1$, otherwise a sizeable deviation could occur, as seen for $c_s \geq 1.5$. Also, the higher one chooses the value of c_s, the more likely it becomes that the resulting crack path deviates from the reference microscale methods results, leading to an inaccurate force-displacement diagram. It appears that this behaves in a chaotic way, where even very slight differences in the initiation of nonlinearities leads to wildly different results in the force-displacement curve and crack pattern advancement, meaning that it is advised that the factor c_s is chosen to be close to or lower than unity.

4. Case study: modeling differential settlement behavior

In this section the proposed multiscale model will be shown in the context of an application, namely the settlement behavior of a masonry wall undergoing gravity and soil erosion [43]. Differential settlement happens when the support under a construction does not settle evenly, causing uneven displacements and often incurring damage in the structure. Studying the mechanisms and influences of the settlement behavior allows us to obtain a better understanding of the failure of several buildings induced by soil settlement, and would allow a means of predicting the behavior of a new construction under settlement behavior. Only recently, more and more research is focusing on how to model damage in masonry under settlement behavior [44, 45, 46].

The example chosen is a long blind wall, shown in Figure 31, undergoing subsidence. This wall consists of 30 by 10 bricks, and starts on a completely flat terrain. The only force acting on the wall is gravity, with the vertical movement bound by the underlying soil function $w(x)$. The same material parameters are used as in Table 2. From the initial point on, there will be a quasi-static lowering of the underlying soil depth driven by the quasi-time variable τ following the function

$$w(x) = \begin{cases} 0 & \text{if } x < x_{\min} \\ w_{\text{end}}(\tau)\left[\cos\left(\pi\dfrac{x - x_{\min}}{x_{\max} - x_{\min}}\right)/2 - 0.5\right] & \text{if } x_{\min} \leq x \leq x_{\max} \\ -w_{\text{end}}(\tau) & \text{if } x > x_{\max} \end{cases} \tag{22}$$

where $x \in [0, 1]$ is the relative horizontal position along the bottom of the wall and the function $w_{\text{end}}(\tau) = \omega_{\text{s}}\tau$ with ω_{s} the step size.

The settling process is shown in Figure 32 at multiple values of w_{end} using the reference microscale model. In this figure the location where elements are supported by the ground are shown in green. From now on unless specified otherwise the values $x_{min} = 0.3$ and $x_{max} = 0.7$ are chosen. One can see a good agreement on the location and evolution of the damaged areas, with the crack path being very similar as well. In Figure 33 the runtimes of the microscale and multiscale model are compared, showing a significant advantage for the multiscale model in this case as well. This shows the applicability of the proposed model to other, more complex, types of examples than just a shear wall.

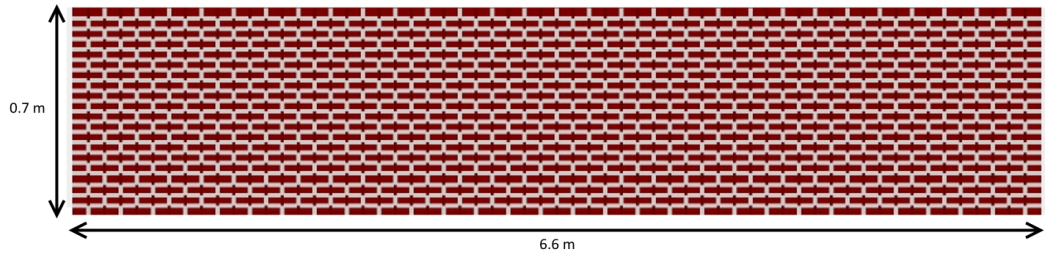

Figure 31: Blind wall setup

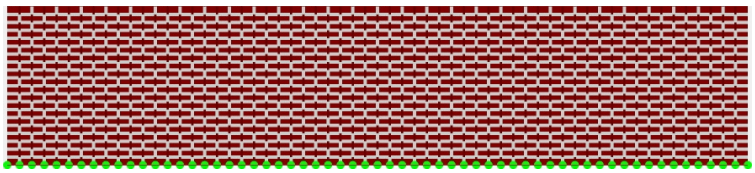

(a) Microscale at $w_{\text{end}} = 0$ mm

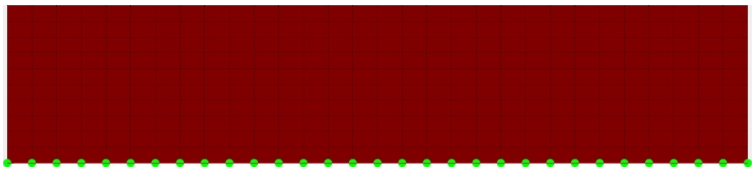

(b) Multiscale at $w_{\text{end}} = 0$ mm

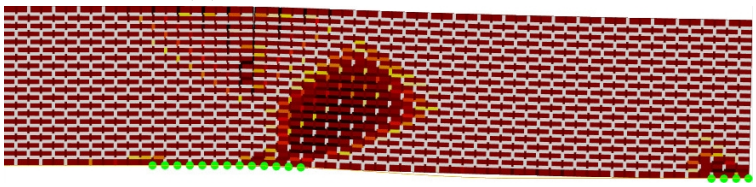

(c) Microscale at $w_{\text{end}} = 1.25$ mm

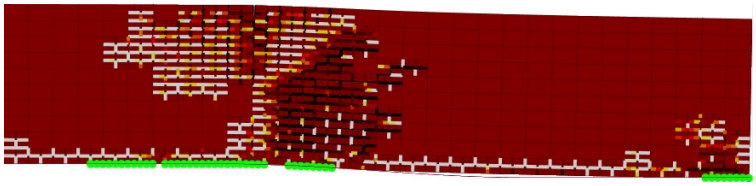

(d) Multiscale at $w_{\text{end}} = 1.25$ mm

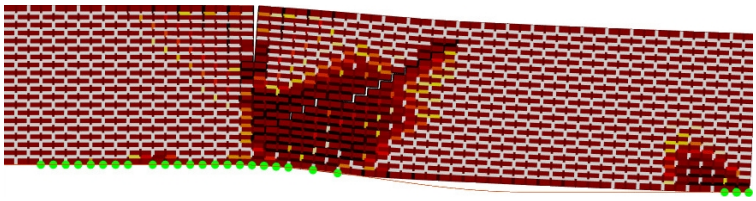

(e) Microscale at $w_{\text{end}} = 2.50$ mm

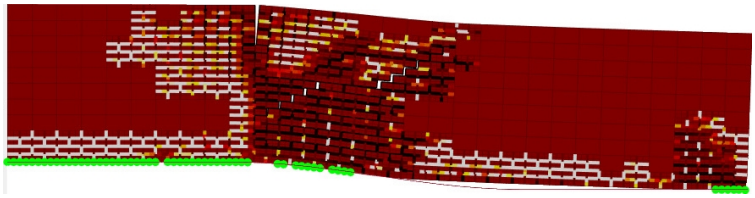

(f) Multiscale at $w_{\text{end}} = 2.50$ mm

Figure 32: Micro- and multiscale settlement at different values w_{end}.

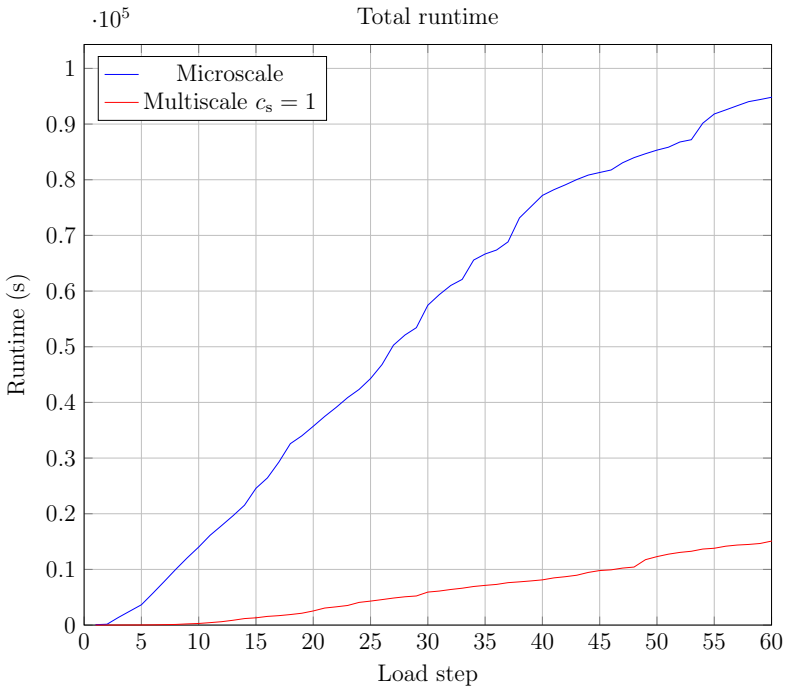

Figure 33: Runtimes of the end settlement models.

5. Conclusions

In this paper, a novel numerical method for modeling large scale masonry structures is presented, and assessed in terms of efficiency and accuracy. It comprises an application of a concurrent multiscale domain activation strategy where one adaptively mixes the use of elastic macroscale elements with nonlinear microscale segments. The main novelty of the method is that this leads to large gains in the necessary computational efficiency, revealing and calculating detailed geometries only when and where required, while keeping the accuracy comparable. Using four example models, a small and two large masonry walls with openings near the center and a case of soil settlement, both the necessary accuracy and efficiency gain of the method are demonstrated. The method is more clearly optimized for large models, like the final two example walls, in which the damage region is minimized compared to the total structure volume. This causes a majority of the wall to remain described by elastic macroscale elements, leading to a larger gain in computational efficiency due to a smaller number of effective degrees of freedom to be taken into account in the simulation. Also at smaller applied displacements the damage is more and more limited, which in itself leads to a higher relative efficiency. In the worst case scenario, meaning the immediate refinement of all macroscale elements due to for example immediate large scale damage initialization, the described multiscale method obtains the same efficiency as a classic microscale method in terms of efficiency.

One also has to find a difficult balance between accuracy and efficiency. By scaling the critical strain surface using the scaling parameter c_s one can optimize this balance. It is seen that for lower values the accuracy of the crack locations goes up, and choosing a value larger than unity is only recommended for systems known by the researcher. In general, for all the example systems, the default value $c_\mathrm{s} = 1$ strikes a good balance between necessary correctness and a low simulation time.

Finally, the results show that masonry modeling is very open to the use of scale embedded multiscale methods. This is mostly due to the localization of nonlinear effects and the small-scale geometric repetition in all relevant dimensions. This makes it both easy to define the RVE itself and divide the model, and keeps the microscale to macroscale ratio low which makes for efficient modeling.

[1] P. B. Lourenço, Computational strategies for masonry structures, Ph.D. thesis, TU Delft, 1996.

[2] A. M. D'Altri, V. Sarhosis, G. Milani, J. Rots, S. Cattari, S. Lagomarsino, E. Sacco, A. Tralli, G. Castellazzi, S. de Miranda, Modeling Strategies for the Computational Analysis of Unreinforced Masonry Structures: Review and Classification, Archives of Computational Methods in Engineering 27 (2020) 1153–1185.

[3] B. Ghiassi, G. Milani (Eds.), Numerical Modeling of Masonry and Historical Structures, Elsevier, 2019.

[4] E. Sacco, D. Addessi, K. Sab, New trends in mechanics of masonry, Meccanica 53 (2018) 1565–1569.

[5] Meillyta, Finite Element Modelling of Unreinforced Masonry (URM) Wall with Openings : Studies in Australia, The Proceedings of 2nd Annual International Conference Syiah Kuala University 2012 & 8th IMT-GT Uninet Biosciences Conference 2 (2012) 236–241.

[6] G. Milani, P. B. Lourenço, A. Tralli, Homogenised limit analysis of masonry walls, Part I: Failure surfaces, Computers and Structures 84 (2006) 166–180.

[7] G. Milani, P. B. Lourenço, A. Tralli, Homogenised limit analysis of masonry walls, Part II: Structural examples, Computers and Structures 84 (2006) 181–195.

[8] G. Milani, A. Tralli, A simple meso-macro model based on SQP for the non-linear analysis of masonry double curvature structures, International Journal of Solids and Structures 49 (2012) 808–834.

[9] S. Marfia, E. Sacco, Multiscale damage contact-friction model for periodic masonry walls, Computer Methods in Applied Mechanics and Engineering 205-208 (2012) 189–203.

[10] G. Milani, Simple homogenization model for the non-linear analysis of in-plane loaded masonry walls, Computers and Structures 89 (2011) 1586–1601.

[11] D. Addessi, E. Sacco, A multi-scale enriched model for the analysis of masonry panels, International Journal of Solids and Structures 49 (2012) 865–880.

[12] G. Wang, S. Li, H.-n. Nguyen, N. Sitar, M. Asce, Effective Elastic Stiffness for Periodic Masonry Structures, Journal of Materials in Civil Engineering 19 (2007) 269–277.

[13] A. Cecchi, K. Sab, A multi-parameter homogenization study for modeling elastic masonry, European Journal of Mechanics, A/Solids 21 (2002) 249–268.

[14] S. Brasile, R. Casciaro, G. Formica, Finite Element formulation for nonlinear analysis of masonry walls, Computers and Structures 88 (2010) 135–143.

[15] S. Brasile, R. Casciaro, G. Formica, Multilevel approach for brick masonry walls Part I: A numerical strategy for the nonlinear analysis, Computer Methods in Applied Mechanics and Engineering 196 (2007) 4934–4951.

[16] S. Brasile, R. Casciaro, G. Formica, Multilevel approach for brick masonry walls - Part II: On the use of equivalent continua, Computer Methods in Applied Mechanics and Engineering 196 (2007) 4801–4810.

[17] T. Hou, X.-H. Wu, A multiscale finite element method for elliptic problems in composite materials and porous media, Journal of Computational Physics 134 (1997) 169–1189.

[18] T. Zahra, M. Dhanasekar, A generalised damage model for masonry under compression, International Journal of Damage Mechanics 25 (2016) 629–660.

[19] P. B. Lourenço, G. Milani, A. Tralli, A. Zucchini, Analysis of masonry structures: review of and recent trends in homogenization techniques, Canadian Journal of Civil Engineering 34 (2008) 1443–1457.

[20] M. De Bellis, D. Addessi, V. Ciampi, A. Paolone, An enhanced first order computational homogenization technique for the study of masonry structures, Handling Exceptions in Structural Engineering (2008) 6.

[21] E. Weinan, Principles of Multiscale Modeling, Physics Today 65 (2011) 56.

[22] K. Heyens, B. Vandoren, L. Schueremans, Multiscale Modeling of Masonry Structures Using Domain Decomposition Techniques, XI International Conference on Computational Plasticity (2011) 422–431.

[23] S. Ghosh, K. Lee, P. Raghavan, A multi-level computational model for multi-scale damage analysis in composite and porous materials, volume 38, 2001.

[24] A. Mobasher Amini, D. Dureisseix, P. Cartraud, Multi-scale domain decomposition method for large-scale structural analysis with a zooming technique: Application to plate assembly, International Journal for Numerical Methods in Engineering 79 (2009) 417–443.

[25] P. Kerfriden, O. Allix, P. Gosselet, A three-scale domain decomposition method for the 3D analysis of debonding in laminates, Computational Mechanics 44 (2009) 343–362.

[26] G. Formica, Multilevel analysis of masonry buildings, Ph.D. thesis, University of Calabria, 2004.

[27] O. Lloberas-Valls, D. J. Rixen, A. Simone, L. J. Sluys, Multiscale domain decomposition analysis of quasi-brittle heterogeneous materials, Phd thesis, TU Delft, 2012.

[28] F. Greco, L. Leonetti, R. Luciano, P. Nevone Blasi, An adaptive multiscale strategy for the damage analysis of masonry modeled as a composite material, Composite Structures 153 (2016) 972–988.

[29] F. Greco, L. Leonetti, R. Luciano, P. Trovalusci, Multiscale failure analysis of periodic masonry structures with traditional and fiber-reinforced mortar joints, Composites Part B: Engineering 118 (2017) 75–95.

[30] B. Vandoren, K. De Proft, A. Simone, L. J. Sluys, Mesoscopic modelling of masonry using weak and strong discontinuities, Computer Methods in Applied Mechanics and Engineering (2013) 167–182.

[31] J. Mazars, G. Pijaudier-Cabot, Continuum damage theory - application to concrete, Journal of Engineering Mechanics 115 (1989) 345–365.

[32] D. C. Drucker, W. Prager, Soil mechanics and plastic analysis or limit design, Quarterly of Applied Mathematics 10 (1952) 157–165.

[33] O. Lloberas-Valls, D. J. Rixen, A. Simone, L. J. Sluys, Domain decomposition techniques for the efficient modeling of brittle heterogeneous materials, Computer Methods in Applied Mechanics and Engineering 200 (2011) 1577–1590.

[34] O. Lloberas-Valls, D. J. Rixen, A. Simone, L. J. Sluys, On micro-to-macro connections in domain decomposition multiscale methods, Computer Methods in Applied Mechanics and Engineering 225-228 (2012) 177–196.

[35] M. Dhanasekar, A. W. Page, P. W. Kleeman, Failure of brick masonry under biaxial stresses, Proceedings of the Institution of Civil Engineers (London) 79 (1985) 295–313.

[36] A. Page, The biaxial compressive strength of brick masonry, Proc. Institution of Civil Engineers 2 2 (1981) 893–906.

[37] A. Page, The strength of brick masonry under biaxial compression-tension, International Journal of Masonry Construction 3 (1983) 26–31.

[38] A. M. D'Altri, S. de Miranda, G. Milani, G. Castellazzi, A numerical procedure for the force-displacement description of out-of-plane collapse mechanisms in masonry structures, Computers & Structures 233 (2020) 106234.

[39] G. Milani, Upper bound sequential linear programming mesh adaptation scheme for collapse analysis of masonry vaults, Advances in Engineering Software 79 (2015) 91–110.

[40] V. P. Nguyen, Multiscale failure modelling of quasi-brittle materials, Ph.D. thesis, TU Delft, 2011.

[41] M. De Bellis, V. Ciampi, S. Oller, D. Addessi, Multi-Scale Techniques for Masonry Structures, 119, CIMNE, 2010.

[42] R. V. D. Pluijm, Material properties of masonry and its components under tension and shear, Proceedings of 6th Canadian Masonry Symposium (1992) 675–686.

[43] B. Vandoren, Discontinuous modelling of masonry failure, Ph.D. thesis, Hasselt University, 2013.

[44] A. Tralli, A. Chiozzi, N. Grillanda, G. Milani, Masonry structures in the presence of foundation settlements and unilateral contact problems, International Journal of Solids and Structures 191-192 (2020) 187–201.

[45] A. Iannuzzo, F. D. Serio, A. Gesualdo, G. Zuccaro, A. Fortunato, M. Angelillo, Crack patterns identification in masonry structures with a C° displacement energy method, International Journal of Masonry Research and Innovation 3 (2018) 295.

[46] S. Tiberti, N. Grillanda, V. Mallardo, G. Milani, A Genetic Algorithm adaptive homogeneous approach for evaluating settlement-induced cracks in masonry walls, Engineering Structures 221 (2020) 111073.